Thermal Kinetic Inductance Detectors for Millimeter-Wave Astrophysics

A. Wandui,[1, a)] J.J. Bock,[1, b)] C. Frez,[2] M. Hollister,[3] L. Minutolo,[2] H. Nguyen,[2] B. Steinbach,[1] A. Turner,[2] J. Zmuidzinas,[1] and R. O'Brient[2, c)]

[1)] *Department of Physics, California Institute of Technology, Pasadena, CA, 91125*

[2)] *Jet Propulsion Lab, Pasadena, CA, 91109*

[3)] *Fermilab, Batavia, IL, 60510*

(Dated: 27 January 2020)

Thermal Kinetic Inductance Detectors (TKIDs) combine the excellent noise performance of traditional bolometers with a radio frequency (RF) multiplexing architecture that enables the large detector counts needed for the next generation of millimeter wave instruments. Here we present dark prototype TKID pixels that demonstrate a noise equivalent power NEP = $2 \times 10^{-17}\mathrm{W}/\sqrt{\mathrm{Hz}}$ with a $1/f$ knee at 0.1 Hz, suitable for background-limited noise performance at 150 GHz from a ground-based site. We discuss the optimizations in the device design and fabrication techniques to realize optimal electrical performance and high quality factors at a bath temperature of 250 mK.

I. INTRODUCTION

The current generation of ground-based millimeter-wave telescopes studying polarization anisotropies in the cosmic microwave background (CMB), employ arrays of thousands of cryogenic Transition Edge Superconducting Sensors (TES) bolometric detectors. A key requirement for measuring the weak CMB polarization signal is that the detectors be background limited. These detectors are read out using arrays of Superconducting Quantum Interference Devices (SQUIDs) that have sufficient bandwidth to read out multiple TESs on a single line with little additional noise. SQUID-based readout architectures that implement either time (TDM)[1,2] or frequency (FDM)[3–5] domain multiplexing have been deployed by multiple experiments.

The next generation of CMB telescopes will require even higher sensitivity. Under background-limited conditions, gains in sensitivity can only be achieved by deploying larger detector arrays. However, SQUID-based TDM or FDM schemes are challenging and expensive to integrate and read creating a significant problem for instruments with 100,000s or more detectors in large focal planes[6].

As a solution to the readout problem, Kinetic Inductance Detectors (KIDs)[7] have been researched as an alternative detector technology to TESs. At radio readout frequencies, large arrays of KID resonators can be easily read out on a single line using frequency domain multiplexing, eliminating the need for the complex SQUID-based readout and assembly. Like KIDs, Thermal Kinetic Inductance Detectors (TKIDs) are a variation of superconducting resonators. As such, they offer the same multiplexing benefits that enable the large detector counts needed. To date, TKIDs have already been developed as energy detectors for X-ray imaging spectroscopy[8] to simultaneously achieve high spatial and energy resolution, but have not been demonstrated as power detectors for millimeter-wave applications.

A TKID is a bolometer in which temperature variations of a thermally isolated island are measured by changes in the kinetic inductance of a superconducting inductor on the island. In contrast to most KID designs, a TKID's absorber that collects the optical power is electrically decoupled from the resonator. This gives TKIDs an additional degree of engineering flexibility since the resonator and the absorber can be optimized independently.

This paper describes the performance dark prototype devices that demonstrate the feasibility of TKIDs for CMB observations. These devices are improved versions of our initial design[9] and demonstrate noise performance appropriate for background-limited ground-based CMB measurements.

II. DEVICE DESIGN AND EXPECTED DESIGN PERFORMANCE

In this section, we present the theoretical predictions that inform our design of TKID bolometers. Drawing from bolometer and KID theory, we discuss the considerations necessary to achieve background limited noise performance. As an aid to the discussion in this section, a schematic of the thermal and electrical circuit of our TKID bolometers is given in figure 1a. A table of variable definitions is also given in the appendix (section VII).

A crucial part of the device design is quantifying the possible sources of noise. In addition to photon noise during observations, we expect detector noise contributions from 4 additional sources: phonon noise, generation-recombination (gr) noise, amplifier noise and two-level system (TLS) noise. Each of these noise terms is well covered in existing literature[7,10,11] and we will therefore focus mainly on the conditions under which the phonon noise is the dominant dark noise term so our devices are well optimized bolometers.

A. Thermal Architecture

Bolometer theory is well established[10,12,13] and we apply it to inform our predictions of TKID performance. There are a few notable distinctions between the operation of TKIDs and

[a)] Electronic mail: awandui@caltech.edu.

[b)] Also at Jet Propulsion Lab, Pasadena, CA, 91109

[c)] Also at Department of Physics, California Institute of Technology, Pasadena, CA, 91125

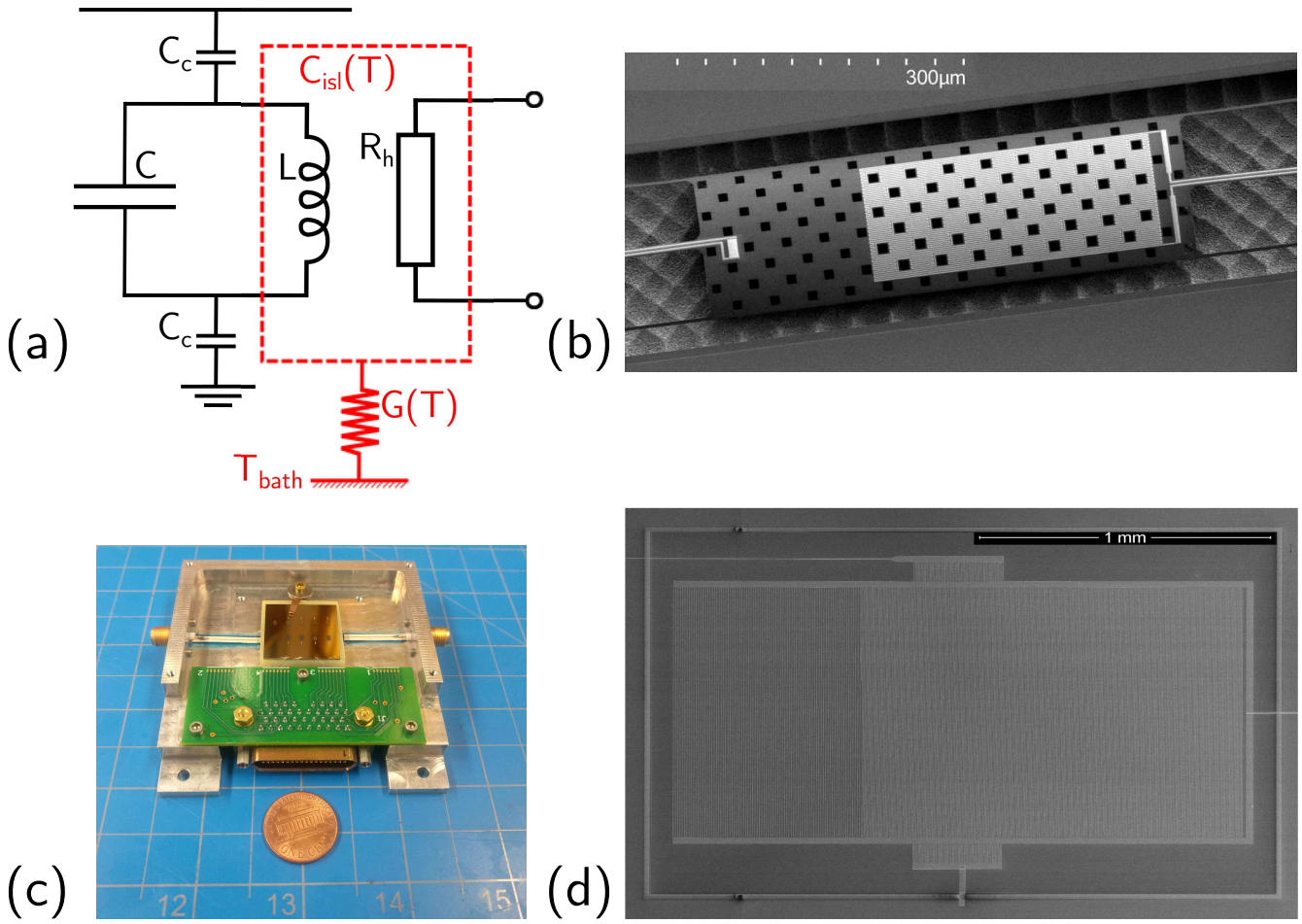

FIG. 1. (a) Schematic of a TKID bolometer. The components in red are the thermal system and those in black are the resonator. R_h represents an Au resistor where we can deposit electrical power to simulate optical loading and to directly measure power responsivity. (b) SEM Micrograph of the released bolometer with the inductor. On the left is the Au heater. (c) Photograph of a single TKID prototype chip with the bias circuit.(d) SEM Micrograph of the TKID capacitor

the more familiar TES bolometers that we will draw attention to in this section.

Like all bolometers, the thermal response of a TKID is governed by the differential equation:

$$C(T)\frac{dT}{dt} = -P_{\rm leg} + P_{\rm read} + P_{\rm opt}, \tag{1}$$

where $C(T)$ is the heat capacity of the thermal island at a temperature, T. Here, $P_{\rm opt}$ is the optical signal power absorbed on the island while $P_{\rm read}$ is the readout power dissipated[14] by the inductor that sits on the island as depicted in figure 1. The net heat flow from the thermal island to the thermal bath may be written as $P_{\rm leg} = K\left(T^{n+1} - T_{\rm bath}^{n+1}\right)$, with K a coefficient and n the power-law index. The thermal conductance of the island legs is the derivative of $P_{\rm leg}$ with respect to the island temperature, $G(T) = (n+1)\,K\,T^n$.

Unlike TES bolometers, we operate TKIDs in the regime where $P_{\rm read} \ll P_{\rm opt}$, and therefore with negligible electrothermal feedback. The equilibrium condition, $P_{\rm opt} = P_{\rm leg}$ sets the operating temperature T_o for a given bath temperature. Since the CMB signal can be described as small fluctuations in the optical power $\delta P_{\rm opt}$, our interest is in the small signal bolometer response δT obtained by expanding equation 1 for small perturbations about the operating temperature. The resulting equation in Fourier space is:

$$\delta T(\nu) = \frac{\delta P_{\rm opt}}{G(T_o)} \cdot \frac{1}{1 + j2\pi\nu\tau_{\rm bolo}}. \tag{2}$$

Here, $G(T_o)$ is the thermal conductance at operating temperature. The bolometer time constant, $\tau_{\rm bolo} = C(T_o)/G(T_o)$, sets the bandwidth of the device, which must be much larger than the science frequency band, i.e. $\nu_{\rm BW} = 1/(2\pi\tau_{\rm bolo}) > \dot{\theta}/\theta_{\rm FWHM}$ where $\dot{\theta}$ is the scan rate and $\theta_{\rm FWHM}$ is the beam size.

Our bolometer design targets a 380 mK operating temperature at a 250 mK bath temperature, accessible with a ^{3}He cooler. This island temperature is set by the choice of material for the inductor and the desired quality factor of the resonators derived from multiplexing considerations. For ground-based observations of the CMB made from the

South Pole at 150 GHz, the expected optical loading, $P_{\rm opt} \sim$ 5pW, requires a thermal conductance of $G(T_o) \sim$ 55pW/K, which is realizable using silicon nitride films with a suitable geometry[15].

The thermal conductance $G(T_o)$ not only sets the response of the bolometer, but also the expected phonon noise level expressed as a noise equivalent power (NEP),

$$\mathrm{NEP}^2_{\rm ph} = 4\chi k_B T_o^2 G(T_o). \tag{3}$$

The factor χ accounts for the temperature gradient across the bolometer legs[10,11]. In comparison, the photon noise for a single-mode detector $\mathrm{NEP}_{\rm photon}$ is given by

$$\mathrm{NEP}^2_{\rm photon} = 2h\nu_{\rm opt}P_{\rm opt} + 2\frac{P^2_{\rm opt}}{\Delta\nu_{\rm opt}}, \tag{4}$$

where $\nu_{\rm opt}$ is the optical frequency and $\Delta\nu_{\rm opt}$ is the optical bandwidth. We can directly compare the phonon and photon noise levels by re-expressing the phonon NEP in terms of the optical loading , $\mathrm{NEP}^2_{\rm ph} = 4\chi\gamma k_B T_o P_{\rm opt}$. For our device parameters, $\chi = 0.57$ and $\gamma = (n+1)/(1-(T_{\rm bath}/T_o)^{(n+1)}) = 4.2$, giving $\mathrm{NEP}_{\rm ph} = 16$ aW$/\sqrt{\rm Hz}$, which is subdominant to $\mathrm{NEP}_{\rm photon} = 43$ aW$/\sqrt{\rm Hz}$ at $\nu_{\rm opt} = 150$ GHz, $\Delta\nu_{\rm opt}/\nu_{\rm opt} = 0.25$. We stress that our device is designed so that phonon noise sets the detector noise limit rather than other noise sources such as quasiparticle gr noise as for KIDs[7].

B. Electrical Properties

Small signal changes in the island temperature are read out by monitoring the forward transmission S_{21} of the TKID resonator. For a resonator with resonant frequency f_r, internal quality factor Q_i, and probed with a tone of frequency f, S_{21}, is given by

$$S_{21} = 1 - \frac{Q_r}{Q_c}\frac{1}{1+j2Q_r x} \tag{5}$$

where $x = (f-f_r)/f_r$ is the fractional shift between the resonance frequency and the probe signal and $Q_r^{-1} = Q_i^{-1} + Q_c^{-1}$. The coupling quality factor, Q_c, is a measure of how well the resonator is coupled to the main feedline. Changes in the island temperature $\delta T(t)$ induce fractional changes in the resonance frequency, $\delta x = (f_r(t) - f_r)/f_r$ as well as changes in the resonator dissipation, $\delta_i = Q_i^{-1}(t) - Q_i^{-1}$. If these fluctuations are slower than the resonator bandwidth $f_r/2Q_r$, we can express the change in the complex transmission at a modulation frequency ν as

$$\delta S_{21}(\nu) = \frac{Q_i}{4}\chi_c\chi_g e^{-2j\phi_g}\left[\delta_i(\nu) + j2\delta x(\nu)\right], \tag{6}$$

where χ_c is the coupling efficiency, which equals 1 at optimal coupling when $Q_i = Q_c$ and therefore, $Q_r = Q_c/2$. χ_g is the detuning efficiency and equals 1 when the probe is tuned to the resonance, i.e. $f = f_r$, in which case $\phi_g = 0$[7].

Whereas KIDs detect non-thermal photo-generated quasiparticles, TKIDs measure the thermal quasiparticle population. In our design, the equilibriation time between the quasiparticles and the bolometer island, $\tau_{\rm qp}$ is rapid compared to the island's thermal time constant $\tau_{\rm bolo}$. In addition, the total quasiparticle density $n_{\rm qp} \approx n_{\rm th}$. In this case, we can predict δx and δ_i from the thermal quasiparticle density, given by BCS theory[16],

$$n_{\rm th} = 2N_0\sqrt{2\pi k_B T\Delta}\cdot\exp\left[-\frac{\Delta}{k_B T}\right]. \tag{7}$$

$\Delta = 1.763 k_B T_c$ is the gap energy for a BCS superconductor with transition temperature T_c and single-spin density of states at the Fermi level N_0. Changes in the quasiparticle density with temperature can be directly related to changes in the resonant frequency and dissipation using the Mattis-Bardeen equations as $Q_i\delta_i = \left(\delta n_{\rm qp}/n_{\rm qp}\right)$ and $Q_i\delta x = \frac{1}{2}\beta(f,T)\left(\delta n_{\rm qp}/n_{\rm qp}\right)$. Here β is the ratio of the frequency response to the dissipation response and is approximated by[7]

$$\beta(f,T) = \frac{1+\sqrt{\frac{2\Delta}{\pi k_B T}}\exp\left[-\frac{hf}{2k_B T}\right]I_0\left[\frac{hf}{2k_B T}\right]}{\frac{2}{\pi}\sqrt{\frac{2\Delta}{\pi k_B T}}\sinh\left[\frac{hf}{2k_B T}\right]K_0\left[\frac{hf}{2k_B T}\right]}. \tag{8}$$

Here, K_0 and I_0 are the zeroth order modified Bessel functions of the first and second order respectively. At our operating temperature, $\beta >> 1$, which means that the resonator frequency shift provides a larger signal for island thermometry than the resonator dissipation.

Chaining the thermal and electrical response gives the full optical responsivity of a TKID bolometer:

$$S \equiv \frac{\delta f_r}{\delta P_{\rm opt}} = \frac{\partial f_r}{\partial x}\frac{\partial x}{\partial n_{\rm qp}}\frac{\partial n_{\rm qp}}{\partial T}\frac{\partial T}{\partial P_{\rm opt}} = f_r(T)\frac{\kappa(T)\beta(f,T)}{2\,Q_i\,G(T)\,T} \tag{9}$$

where

$$\kappa(T) \equiv \frac{\mathrm{d}\ln n_{\rm qp}}{\mathrm{d}\ln T} = \left(\frac{1}{2} + \frac{\Delta}{k_B T}\right).$$

The responsivity can thus be directly estimated using measured quantities at a known island temperature.

C. Other Noise Terms

We now turn our attention to the three remaining noise terms: gr, TLS, and amplifier noise from the readout chain. All the noise terms add in quadrature: $\mathrm{NEP}^2_{\rm total} = \mathrm{NEP}^2_{\rm photon} + \mathrm{NEP}^2_{\rm ph} + \mathrm{NEP}^2_{\rm gr} + \mathrm{NEP}^2_{\rm amp} + \mathrm{NEP}^2_{\rm TLS}$. We consider each of these terms in turn and describe the conditions under which each of them remains sub-dominant to the phonon noise level.

Generation-recombination noise arises because quasiparticle production and recombination are random processes that

fluctuate over time. Even so, the dynamics of the ensemble averaged quasiparticle population, $\langle N_{\rm qp}\rangle$ are well described by using non-equilibrium statistical mechanics[17].

TKIDs operate at large quasiparticle densities where the recombination rate $\langle\Gamma_{\rm rec}\rangle$ is expected to be quadratic in quasiparticle density,

$$\langle\Gamma_{\rm rec}\rangle = \frac{1}{2}V_{\rm sc}\, R\, n_{\rm qp}^2 \tag{10}$$

Here, R is the recombination constant at the superconductor. For small perturbations in the quasiparticle density about its mean value, quasiparticles have a characteristic lifetime $\tau_{\rm qp} = 1/\left(Rn_{\rm qp}\right)$. Meanwhile, the quasiparticle number fluctuations can be described by a one-sided power spectrum $S_{\rm gr}(\nu)$ of quasiparticle number fluctuations given as[17]

$$S_{\rm gr}(\nu) = \frac{4\tau_{\rm qp}\, n_{\rm qp}\, V_{\rm sc}}{1+(2\pi\nu\tau_{\rm qp})^2}. \tag{11}$$

We can obtain the expected generation-recombination NEP by dividing the power spectrum by $V_{\rm sc}^2\cdot\left(\partial n_{\rm qp}/\partial P_{\rm opt}\right)^2$ and taking the square root,

$$\mathrm{NEP}_{\rm gr} = \frac{2G(T)T}{n_{\rm qp}(T)\,\kappa(T)}\cdot\frac{1}{\sqrt{R\,V_{\rm sc}}}. \tag{12}$$

Equation 12 shows that at high temperatures, gr noise is suppressed because the quasiparticle density increases exponentially with temperature. In addition, the responsivity, given in equation 9, is independent of the superconductor volume, and so we are free to make the inductor volume $V_{\rm sc}$ large to further suppress the gr noise. This is an additional degree of flexibility for TKIDs, unlike many KID designs in which the inductor volume must be kept small to keep the optical responsivity high[7,18]. The freedom to use a large inductor volume also allows us to use lower readout frequencies at a fixed capacitor size or alternatively, use smaller capacitors to achieve the same readout frequency.

Unlike the noise terms already considered, we must rely on semi-empirical scaling model available to predict the expected TLS noise level. TLS noise is sourced by random fluctuations in the dielectric constant of amorphous materials that couple to the electric field in the resonator. These amorphous dielectrics also modify the quality factor and introduce an additional temperature-dependent frequency shift given by

$$Q_{\rm TLS}^{-1} = F\,\delta_{\rm TLS} = F\,\delta_0\tanh\left(\frac{hf}{2k_BT}\right)\cdot\frac{1}{\sqrt{1+P_g/P_c}}, \tag{13}$$

$$x_{\rm TLS} = \frac{F\,\delta_0}{\pi}\left[\mathbb{R}\mathrm{e}\left[\Psi\left(\frac{1}{2}+\frac{hf}{2j\pi k_BT}\right)\right]-\ln\left(\frac{hf}{k_BT}\right)\right]. \tag{14}$$

Here, $\delta_{\rm TLS}$ is the TLS contribution to the dielectric loss tangent, F is a filling factor that accounts for the fraction of the total electrical energy of the resonator that is stored in the TLS hosting material and δ_0 is a constant[7,19] and Ψ is the digamma function[19]. At a probe tone power P_g and tone frequency f, TLS effects introduce a power dependence to the quality factor characterized by a critical power P_c. In addition, the fractional frequency shift is expected to be only weakly power dependent and positive with temperature increase. However, for $k_BT \ll hf$, the TLS loss drops off as $1/T$ such that we expect that at our operating temperatures, our resonators will be well characterized using only the Mattis Bardeen relations.

In order to make predictions of the TLS noise, we parametrize the power, frequency and temperature dependence of the TLS power spectrum $S_{\rm TLS}$ as[19]

$$S_{\rm TLS}\left[\mathrm{Hz}^{-1}\right] = \kappa_0\left(\frac{\nu}{300\mathrm{MHz}}\right)^{-\alpha}\left(\frac{T}{380\mathrm{mK}}\right)^{-\beta}(1+N/N_c)^{-\gamma}, \tag{15}$$

where $\alpha = 1/2, \beta = 1.5-2$ and $\gamma = 0.5$[7] . Here $N = E/(hf_r)$ is the microwave photon number, with $E = \frac{1}{2}\cdot Q_i\chi_c\chi_g\cdot P_g/(2\pi f_r)$, representing the energy stored in the resonator. Other values for the exponents α and β, have been measured or suggested[20–23]. We estimate $N_c \sim 7\times10^6$ from measured TLS critical powers at our devices, $P_c \sim -95$ dBm. A few simple scaling relations between $\delta_{\rm TLS}$ and $S_{\rm TLS}$, which would be immensely useful for predicting TLS behavior, have also been reported in literature[21–23]. We do not refer to these but instead considered measured noise levels for similarly designed devices that were presented in Figure 14 of Ref 7. We then scaled these to our temperature and frequency range of interest and expect at worst case, $S_{\rm TLS}(1\mathrm{Hz}, T_o, -90\mathrm{dBm}) \sim 4\times10^{-19}\,\mathrm{Hz}^{-1}$.

We can obtain the TLS NEP by dividing the power spectrum by the responsivity

$$\mathrm{NEP}_{\rm TLS}^2 = \frac{1}{\left(\partial x/\partial P_{\rm opt}\right)^2}S_{\rm TLS}. \tag{16}$$

For the condition $\mathrm{NEP}_{\rm TLS}^2 \ll \mathrm{NEP}_{\rm ph}^2$ to hold at our operating temperature, we find that

$$S_{\rm TLS} \ll 4\chi k_BT_o^2G(T_o)\left(\frac{\partial x}{\partial P_{\rm opt}}\right)^2 \approx 2.7\times10^{-17}\,\mathrm{Hz}^{-1}. \tag{17}$$

This condition holds because our TKIDs have a high responsivity, $\partial x/\partial P_{\rm opt} = 331$ ppm/pW^{-1}, at the operating temperature. The two orders of magnitude gap between the expected TLS noise level and the upper tolerable limit gives us good confidence that TLS noise will have negligible impact on our devices during normal operation.

Lastly, we consider the amplifier noise. For an amplifier with noise temperature T_N and with probe power P_g, the NEP contribution is given by

$$\mathrm{NEP}_{\rm amp} = \frac{1}{S}\cdot\frac{Q_c}{2\,Q_r^2}\sqrt{\frac{2k_BT_N}{P_g}}. \tag{18}$$

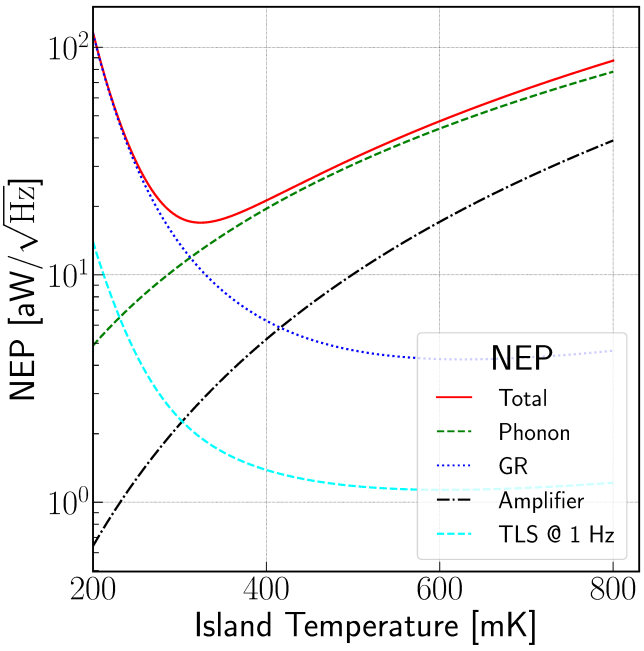

FIG. 2. Internal noise of an aluminum TKID as a function of the island temperature. For predicting the TLS noise, $\kappa_0 = 8 \times 10^{-23}$ Hz^{-1}.

The amplifier noise contribution can be made small by using a low-noise amplifier and by biasing the resonators with a large readout power. Cryogenic low noise amplifiers with $T_N < 10$ K are readily available commercially. However, we deliberately limit the bias power to avoid having to account for non-linearity in the kinetic inductance.

An optimized bolometer has detector noise contributions, $\mathrm{NEP_{gr}}$, $\mathrm{NEP_{TLS}}$ and $\mathrm{NEP_{amp}}$ below the phonon noise. Figure 2 shows a breakdown of the noise terms for an aluminum TKID as a function of the island temperature. The figure shows the limits under which generation-recombination vs. phonon noise dominates in the resonator. The bolometer parameters were chosen to be suitable for 150 GHz ground-based observations of the CMB.

D. Device Design

We can apply the results from the previous subsections to determine an optimal design for TKID bolometers. First, since the phonon noise term dominates the internal noise, then the internal noise at the operating temperature is only a weak function of T_c. This means that a wide range of materials with T_c in the range $0.8 - 2$ K can be used as background-limited detectors. We chose Aluminum with $T_c = 1.2$K as our superconductor for ease of fabrication. Using higher T_c materials could offer a multiplexing advantage because Q_r at the operating temperature increases with T_c.

Motivated by the desire to reduce the cost of readout electronics, we designed devices with relatively low resonance frequencies around 300 MHz. We designed each test chip with 5 TKIDs with a 15 MHz frequency spacing between resonators. The resonator circuits are built out of lithographed, lumped element inductors and capacitors. A fixed inductor geometry was used for all the devices and each resonator has a unique main capacitor that sets the resonant frequency. Smaller coupling capacitors are used to set the coupling of the resonator to the readout line. Niobium with $T_c = 9$ K was used for all the capacitors and feedline structures so that the thermal response is solely attributable to the aluminum inductor. Figure 1 shows a simplified schematic of a TKID as well as a scanning electron microscope image of the bolometer island with the inductor and heater in view.

III. DETECTOR FABRICATION

Our approach to the fabrication of these TKID bolometers, leveraged the long heritage in making TES bolometers for CMB observations under the BICEP/Keck experiments. All the devices were fabricated and tested at JPL.

We fabricate the bolometers on 500 μm thick, high resistivity Si wafers. A Low Stress Silicon Nitride (LSN) layer and a SiO_2 inter-layer dielectric (ILD) layer are deposited over the silicon. The LSN layer is then patterned to make the thermal island. We suspend the island over a hole etched into the silicon using six LSN legs. These legs make the weak thermal link from island to wafer. By selecting the length of the bolometer legs, we can also tune the thermal conductance. On each test chip, one device was fabricated with no island and the other 4 with bolometer leg lengths 100 μm, 200 μm, 300 μm and 400 μm. We fixed the island size to $\sim$100 μm by $\sim$500 μm for all the devices. The expected heat capacity is 0.059 pJ/K, accounting for the dielectric (LSN and ILD) and metal (Nb and Al) layers[24–26]. The heat capacity is set by island volume of about 30,000 μm^3, which is much larger than the combined volume of the bolometer legs of about 5,000 μm^3 for the longest leg bolometer. As a result, we expect that all the devices would have the same the heat capacity. Measurements of the thermal conductance need calibration and so we placed a small gold resistor on the island that could be biased using an external circuit to deposit a set amount of power on the island (see Figure 1 (b)).

The aluminum layer of the inductor is deposited and patterned on the LSN . The meandered inductor traces have width $w \sim 1$ μm wide with $\sim$1 μm spacing between the lines. Sonnet[27] simulations done assuming a surface inductance $L_s = 0.27$ pH/$\square$, give a predicted geometric inductance, L_g of about 5 nH and a kinetic inductance fraction, $L_k/(L_k + L_g) = \alpha_k = 0.42$, where $L_k = L_s \cdot (l/w)$ is the kinetic inductance for a total inductor length l. The low film resistivity of Aluminum limits the kinetic inductance fraction. The inductor has a volume of 810 μm^3.

The inter-digitated capacitors (IDC) sit off the island and directly on the crystalline Silicon wafer. The bare silicon is exposed by etching a large via through the ground plane (GP) and LSN layers. We did this to reduce the presence of amorphous dielectric that hosts two-level system[19] (TLS) effects from the capacitors. The via is large to minimize stray

capacitive coupling between the ground plane and the edges of the capacitor, as determined by Sonnet simulations. Two smaller coupling IDCs were placed on opposite sides of the main capacitor to couple the resonator to the readout line and to ground. A second smaller via through the ILD layer makes the contact between the coupling capacitor and the ground plane. The capacitors were patterned using etching instead of liftoff to avoid flags that can potentially host TLS effects.

IV. EXPERIMENTAL SETUP

We tested the devices in a Model 103 Rainier Adiabatic Demagnetization Refrigerator (ADR) cryostat from High Precision Devices (HPD)[28] with a Cryomech PT407 Pulse Tube Cryocooler[29]. We used an external linear stepper drive motor to run the Pulse Tube in order to avoid RF pulses from a switching power supply. For mechanical stiffness, the ultra cold (UC) and intra cold (IC) stages of the cryostat are supported using long diameter Vespel tubes between the 4K stage and the IC and stiff titanium 15-3 alloy X-shaped crossbars between the IC and UC stages. Copper heat straps make the thermal contacts between the stages and the cold heads. The ADR reached a base temperature of 80 mK on the UC stage when the test chip was installed.

The RF connections between the UC and IC stages are through Niobium-Titanium (NbTi) coaxial cables with 10dB, 20dB and 30dB attenuators installed at the UC, IC and 4K stages respectively on the transmit side. At each thermal stage, the coaxial connections are heat sunk to the stage. A cold Low Noise Amplifier (LNA) is mounted at the 4K stage. The cold LNA is a SiGe HBT cryogenic amplifier from Caltech (CITLF2)[30] with a measured noise temperature of 5.2 K with a 1.5 V bias. We also use a second amplifier with a noise temperature of 35 K at 5.0 V bias at room temperature.

For our data acquisition, we used the JPL-designed GPU accelerated system built on the Ettus Research USRP software defined radio (SDR) platform[31]. 10 Gbit Ethernet connects the SDR to an Nvidia GPU, which handles the computationally heavy demodulation and analysis tasks in place of an FPGA. The SDR platform uses a 14 bit ADC and a 16 bit DAC and provides 120 MHz RF bandwidth.

The Al chip holder was sealed up with Aluminum tape to make it light tight[32]. In addition, we anchored a Nb plate onto the UC stage to provide some shielding of the chip from the magnetic field of the ADR magnet.

V. RESULTS

For the device discussed here, we achieved a yield of 4/5 resonators. All the resonances were found in the frequency range 300-360 MHz and with close to the 15 MHz design spacing. The heaters of the 300, 200 and 100 μm leg bolometers were wired up to make calibrated noise and responsivity measurements.

A. Film Properties

Using four-point measurements of an unreleased Al inductor on chip, we measured $T_c = 1.284\ K$, implying a superconducting gap energy, $\Delta = 1.763\ k_B\ T_c = 1.95 \times 10^{-4}$ eV. Using the sheet resistance, $R_s = 0.25\ \Omega/\square$. R_s and Δ gives a surface kinetic inductance, $L_s = \hbar R_s/\pi\Delta$ is 0.27 pH/$\square$. This value of L_s and accounting for the geometric inductance from simulations, gives an expected kinetic inductance fraction, $\alpha_k = 0.42$.

B. Resonator Properties and Modeling

We initially characterized the resonators using readout power sweeps at a fixed bath temperature of 80 mK and varying the power in the range, -110 dBm to -80 dBm. A key goal of this measurement was to determine the power level at the onset of the kinetic inductance non-linearity. In addition, changes in the quality factor with readout power probe two-level system effects.

When fitting the forward transmission S_{21} using the nonlinear resonator model[33], we found it necessary to also account for the asymmetry in the resonator profile[34]. Our model for S_{21} as a function of frequency f for a resonance with resonant frequency f_r is given by

$$S_{21}(f) = Ae^{j\phi_0}\exp\left[j2\pi(f-f_r)D\right]\left(1-\frac{\delta_e}{\delta_r - j2x}\right), \quad (19)$$

where $\delta_r = Q_r^{-1}$, $\delta_e = Q_e^{-1}$ with Q_e, the complex coupling quality factor, $Ae^{j\phi_0}$ is simply a complex scaling of S_{21}, and D is the line delay. The real and imaginary parts of δ_e were used as independent parameters in the fitting. The nonlinear response is accounted for by setting $x = \delta_r y$, where $y = y_0 + a/\left(1+4y^2\right)$, $y_0 = (f-f_r)/f_r$ and a is the bifurcation parameter. a is an independent parameter in the fitting. The internal quality factor Q_i, is recovered from the fitting by $Q_i = \left(\delta_r - \mathbb{R}e\left[\delta_e\right]\right)^{-1}$.

The resonator asymmetry is captured by the phase of Q_e, ϕ_c. For our resonators, we found ϕ_c to be large; in the range $0.4-0.7$ radians. As tested by further simulations, we believe that a large part of the asymmetry is due to 7 pF of capacitive loading from short lengths of transmission line that branch from the readout line to the coupling capacitors.

Even up to the highest powers we probed, $a < 0.8$, implying that the resonators were always below the threshold for the bifurcation[33]. We chose a readout power of -90 dBm for all the subsequent measurements discussed in this paper, well within the linear regime of our devices.

Q_i as a function of both the readout power P_g and temperature T is given by

$$Q_i^{-1}(T,P_g) = Q_{i,0}^{-1} + Q_{\mathrm{MB}}^{-1}(T) + Q_{\mathrm{TLS}}^{-1}(T,P_g), \quad (20)$$

where $Q_{\mathrm{TLS}}^{-1}(T,P_g)$, is given in equation 13 and $Q_{\mathrm{MB}}^{-1}(T)$ is the Mattis-Bardeen prediction[7] and the third parameter $Q_{i,0}$ captures the saturation of Q_i at high power. At 80 mK, the MB

term is negligible and can be ignored for the power sweep measurements. Figure 3 shows Q_i as a function of the readout power for 4 yielded resonators. All four resonators have the product $F\delta_0 \approx 4.6\times10^{-5}$. Three of the resonators have $P_c \approx -95.7$ dBm and $Q_{i,0} \approx 4.4\times10^5$. The 305.9 MHz resonator has lower $Q_{i,0}$ and P_c because of the lower Q_i measured. Consistent with the TLS prediction, we found the fractional frequency shift with power to be negligibly small, peaking at about 5 ppm. Even so, TLS does not fully explain the power dependence on its own because we found that the $Q_{i,0}$ parameter to be necessary in order to obtain good fits. However, $Q_{i,0}$ has not been physically motivated. A possible explanation is that the power dependence is complicated by non-equilibrium quasiparticle distribution effects but this is still an area of active investigation[35,36].

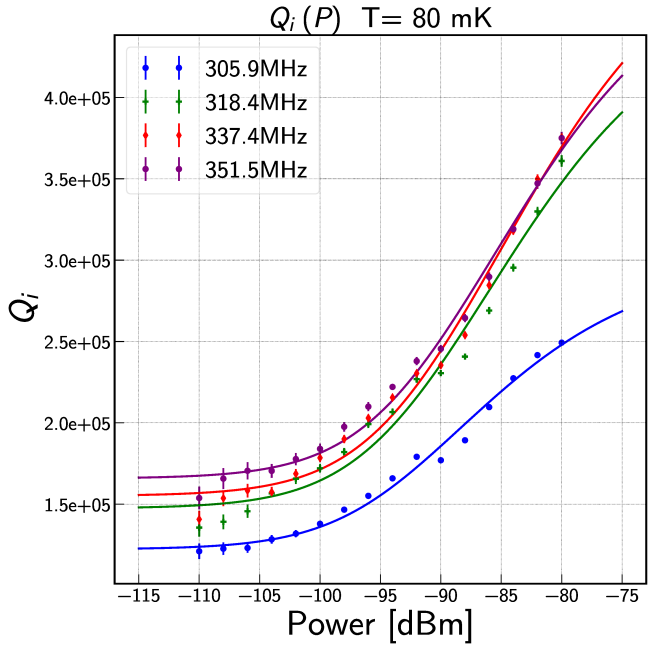

FIG. 3. Internal quality factor Q_i as a function of the readout power at 80 mK. The dots are the data and the solid lines are the fits to the data using the model described in equation 20

We followed up the power sweeps with bath temperature sweeps done at -90 dBm. The temperature sweep was done up to 460 mK, high enough to break the degeneracy between the two parameters, α_k and T_c. At our operating temperature, these two parameters are sufficient to describe our data as shown in figures 4 and 5 which summarize the fit results for the 337.4 MHz resonator.

At the low temperature limit, the MB prediction is complicated by the saturation of the quality factor. We compared three different models to describe this regime: a pure MB prediction, a MB + TLS model and lastly, a model assuming a background quasiparticle prediction but no TLS. All three models were fit to only the frequency shift data and the best fit parameters were then used to make predictions of the internal quality factor. The MB + TLS model predicts a product $F\delta_0 \approx 3.4\times10^{-5}$ for all 4 resonators. However, this value of the loss tangent is too small and gives an incorrect temperature dependence for Q_i at the low temperature limit. Instead, we found that the saturation of Q_i below 200 mK was better captured by assuming we had an excess background quasiparticle population $n_{\rm bg}$. The total quasiparticle density in this case is given by

$$n_{\rm qp} = \sqrt{\left(n_{\rm th}+n^*_{\rm qp}\right)^2 + n^2_{\rm bg}} - n^*_{\rm qp} \tag{21}$$

$n^*_{\rm qp}$ is the crossover density at which the quasiparticle lifetimes in superconductors have been experimentally observed to saturate[7]. Since thermal and excess quasiparticles are equivalent[37], we can describe combined the effect of having both by defining an effective temperature $T_{\rm eff}$ of the system as the temperature at which the total quasiparticle density (equation 21) equals the density of purely thermally generated quasiparticles. We substitute the effective temperature for all temperature dependent terms that determine the frequency shift and loss. $n_{\rm bg}$ is an additional parameter in the fitting. We did not measure $n^*_{\rm qp}$ directly for these devices, but we fixed based on quasiparticle lifetime measurements done on similar TKIDs we fabricated for which $n^*_{\rm qp} = 500$ um^{-3} and $R = 11$um^{3}s^{-1}. Both the pure MB and the MB + TLS models give $T_c \approx 1.38$K and $\alpha_k \approx 0.55$, much higher than the prediction from the film measurements. With the background quasiparticle model, we obtain $T_c \approx 1.32$K and $\alpha_k \approx 0.45$.

On average over the 4 resonators $n_{\rm bg} \approx 700$ um^{-3} corresponding to an effective temperature of about 150 mK. We estimate the recombination power, $P_{\rm recomb}$ from this population of quasiparticles as $P_{\rm recomb} = \frac{1}{2}\Delta\cdot R\cdot n^2_{\rm qp}\cdot V_{\rm sc} = 18$ pW. This estimate of the power dissipation in the superconductor is larger than both the readout power and the heater power we dissipate on the bolometer island. The full understanding of the quasiparticle dynamics at low temperatures in TKIDs as in many other KIDs is still incomplete but this does not affect TKID performance since our target operating temperature, $T_o = 380$ mK is well in the regime where our devices are fully characterized.

C. Thermal Conductivity and Bolometer Time Constants

By fixing the bath temperature and changing the power dissipated biasing the heaters on the thermal island, we can directly measure the bolometer conductance and time constant.

The bath temperature, $T_{\rm bath}$ was fixed at 97 mK and S_{21} was measured at each bias power, P, as the bias power was changed. The shift in resonance frequency was used to predict the island temperature T using the known α_k and Δ. We then fit the island temperature and bias power data to obtain the thermal conductivity coefficient K and power law index n.

Consistent with other similar bolometers used in BICEP/Keck[15], we measured $n \sim 2$. An index $n < 3$ indicates that phonon system has reduced dimensionality. We can motivate this physically, under the assumption that ballistic phonon propagation dominates over scattering in

f_r [MHz]	Q_c	ϕ_c [rad]	$T_c[K]$	α_k	$n_{\rm bg}[{\rm um}^{-3}]$	K [pW/K^{n+1}]	n	C_0 [pJ/K$^{\eta+1}$]	η
305.9	15164 ± 72	0.6455 ± 0.0035	1.33 ± 0.01	0.46 ± 0.01	708 ± 10	352 ± 2	1.962 ± 0.009	1.943 ± 0.213	1.920 ± 0.115
318.4	17675 ± 104	0.7601 ± 0.0034	1.32 ± 0.09	0.45 ± 0.01	711 ± 10	165 ± 1	1.754 ± 0.012	1.839 ± 0.325	1.945 ± 0.184
337.4	22556 ± 129	0.7526 ± 0.0037	1.32 ± 0.01	0.45 ± 0.01	627 ± 9	122 ± 1	1.862 ± 0.011	1.742 ± 0.380	1.914 ± 0.219

TABLE I. Summary of the measured parameters of 3 TKID bolometers. The error bars on Q_c and ϕ_c were obtained from the spread in Q_e over powersweeps. α_k, T_c, were obtained from the bath temperature sweep data fit with a MB + background quasiparticle model. The K and n values reported here are from measurements done at a 250 mK bath temperature.

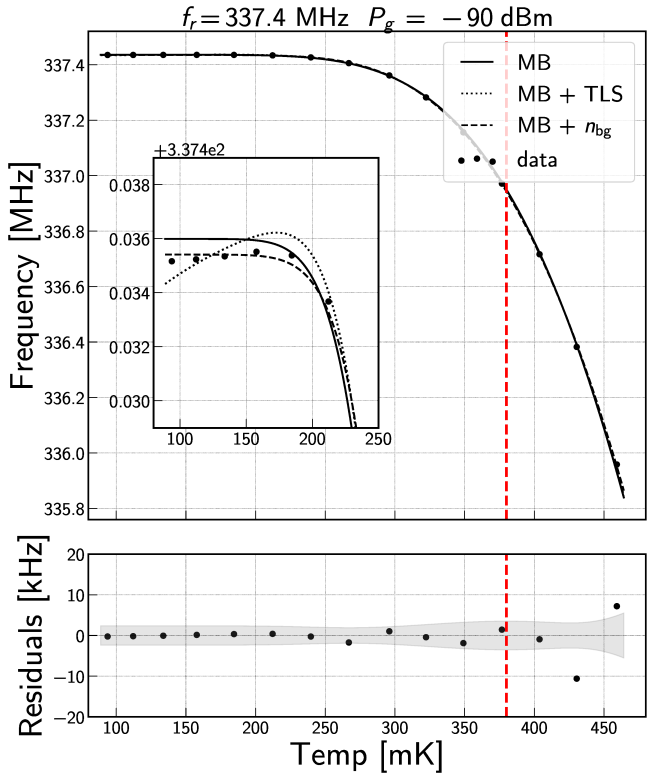

FIG. 4. Fits of the frequency shift data for the 337.4 MHz resonator to three different models: only MB, MB + TLS and MB + a background quasiparticle density. The inset plot has a much smaller x-axis range to better show the differences in the fits at low temperatures. The lower plot gives the fit residuals (black dots) and the one-sigma uncertainty in the fit (gray) for the MB + background quasiparticle model. The red dashed line is our target operating temperature of 380 mK.

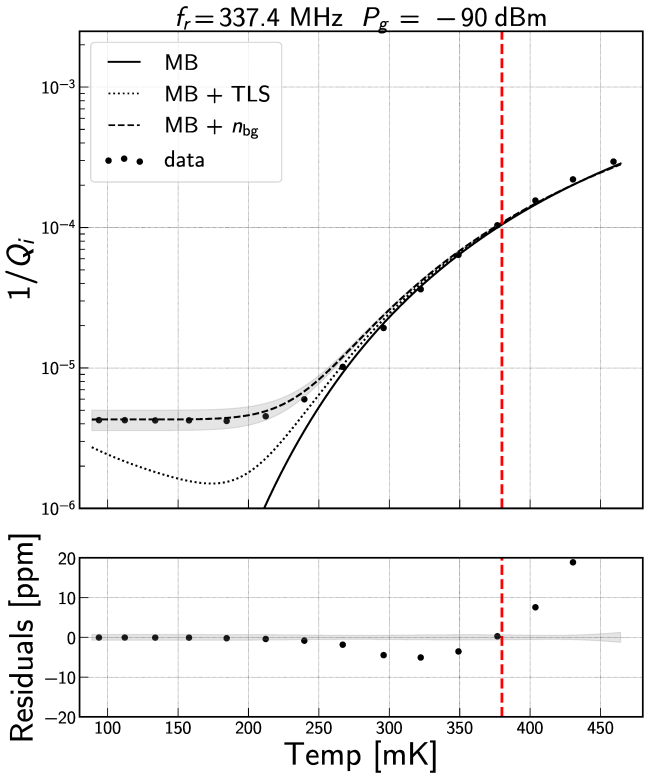

FIG. 5. showing good agreement with the best fit prediction for Q_i^{-1} obtained from fitting the frequency shift data to a MB model assuming a background quasiparticle population. The lower plot gives the fit residuals (black dots) and the one-sigma uncertainty in Q_i^{-1} (gray) from the fit.

thermal transport. In this limit, the thermal phonon wavelength is given by $\lambda_{\rm ph} = hc_s/k_BT$ where c_s is the speed of sound[15]. We expect $\lambda_{\rm ph}$ to vary from 3.5 μm at the 90 mK cold end to about 0.5 μm at the 450 mK hot end for a speed of sound, $c_s \sim 6500$ ms^{-1} in silicon nitride. The nitride layer is only 0.3 μm thick but the legs are 10 μm wide and 300 - 500 μm long, we expect thermal behavior consistent with a 2 dimensional phonon gas. The longitudinal sound velocity in silicon dioxide is comparable to that of silicon nitride so the same argument holds for thermal conduction through the similarly thick ILD layer. With the different bolometer leg lengths on the chip, we verified that the coefficient K, scales inversely with the bolometer leg length as shown in Table I.

As an additional step, we repeated the thermal conductivity measurements at a second bath temperature, 249 mK. The extracted parameters were consistent with each other to about 10 %.

We define the optimal power $P_{\rm optimal}$ as the power needed to achieve the target island operating temperature, $T_o = 380$ mK. $P_{\rm optimal}$ is dependent on the bath temperature and is chosen so that the saturation power equals the expected loading seen during actual observations. At a 250 mK bath temperature, the 300 μm bolometer with a resonant frequency of 337.4 MHz has $P_{\rm optimal}$ appropriate for the expected loading at the South Pole at 150 GHz as shown in figures 6. The 100 μm and 200 μm designs are suitable for operating at 270 GHz and 220 GHz respectively.

We measured the bolometer time constants using a DC bias voltage plus an additional sine wave excitation was applied

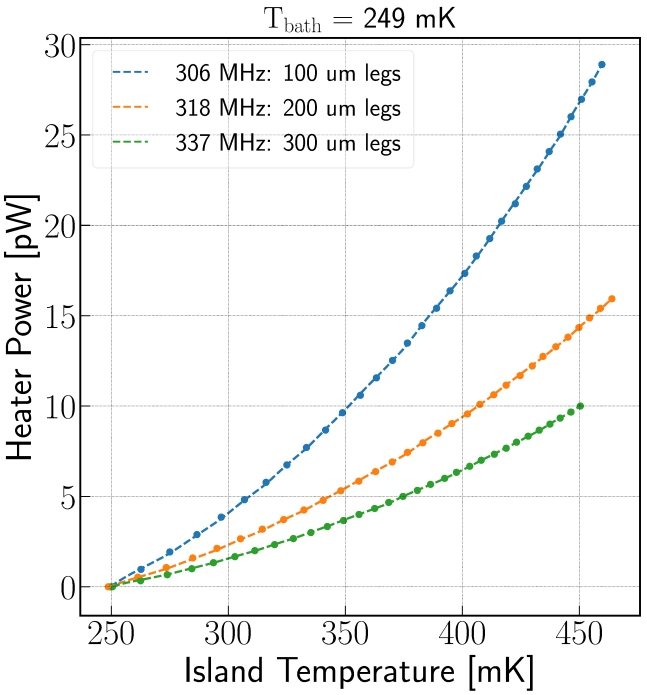

FIG. 6. Heater power plotted against the island temperature for 3 TKIDs showing agreement between the data (points) and best fit model (lines). The data was taken at a 250 mK bath temperature. The difference in slopes between the 3 curves is due to the difference in thermal conductivity of the three bolometers.

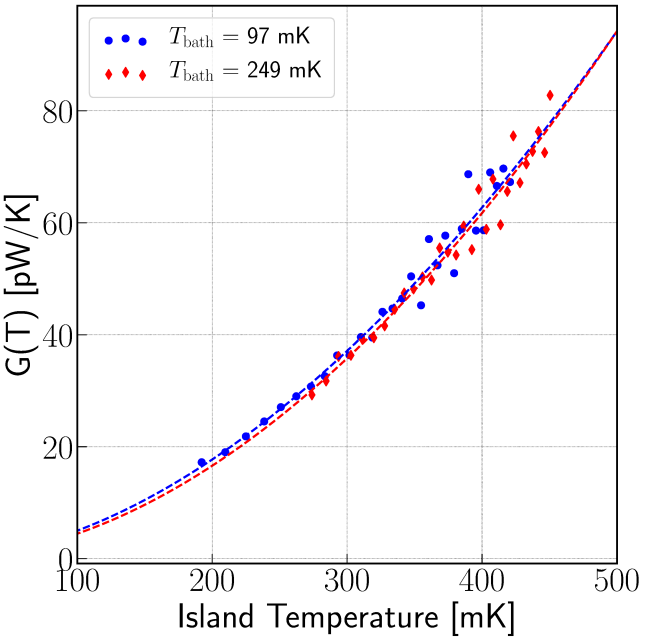

FIG. 7. Comparison of the extracted thermal conductance at 2 bath temperatures. The measurements are given as the filled blue circles and red diamonds while the best fit results are given by the dotted lines. As expected, the thermal conductance is independent of the bath temperature. The results presented here are for the 337 MHz bolometer with 300 um legs.

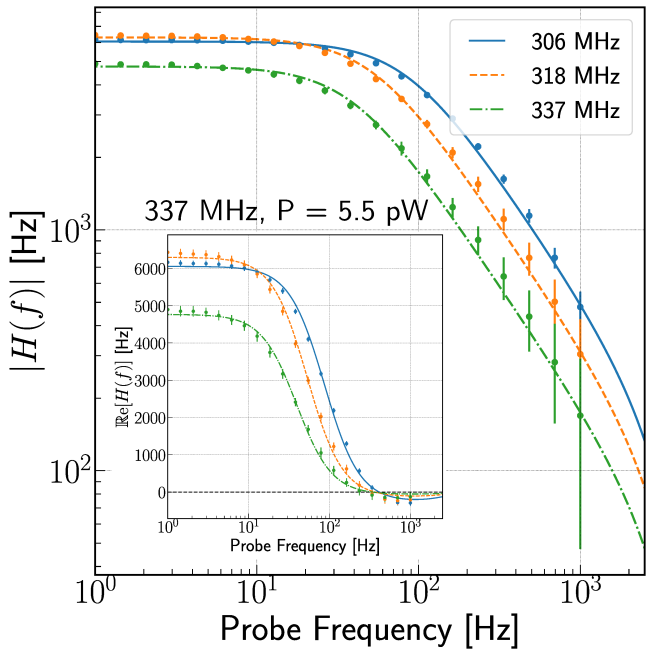

FIG. 8. A comparison between the magnitude and the real part of the bolometer transfer function measured at an 85 mK bath temperature and heater power of 5.5 pW for the 337 MHz bolometer. The data points have error bars enlarged by a factor of 10. The solid lines show the best fit to the model in equation 9. Inset is the real part of the bolometer response showing that response is modulated by the data filtering and additional time delays.

across the heater. The amplitude of the sine wave was about 1 % of the DC bias voltage. In addition, we synchronized the start of the data acquisition to the start of the sine wave excitation so that the phase of the input wave was always known. At each bias power, we stepped the excitation frequency of the input sine wave, f_{exc}, from 1 Hz to 1000 Hz in 30 logarithmically spaced steps.

We convert from the raw I/Q timestreams to resonance frequency and quality factor timestreams using the measured S_{21} parameters. By fitted the amplitude and phase of the change in resonance frequency with time, we obtained the complex bolometer transfer function, $H(f_{exc})$ which we model as a single-pole low-pass filter with rolloff frequency $f_{3dB} = 1/2\pi\tau_{bolo}$. The measured transfer function also includes the effect of the anti-aliasing filter used to decimate the data as well as unknown time delays in the trigger signal from the USRP to the function generator. Figure 8 show the magnitude of the bolometer response with the single pole rolloff.

From these measurements, we conclude that the time constant for the 337 MHz TKID, $\tau \sim 4.5$ms is fast enough for ground-based degree scale CMB observations. Interestingly, the time constants are weakly dependent on the island temperature. We expect the heat capacity to follow a simple power law $C = C_0 T^{\eta}$ and given that $\tau = C/G$, then this implies that $C \sim T^2$ as summarized in table I. Figure 9 confirms that the bulk of the heat capacity is from the island itself and not the bolometer legs. Additionally, the thermal island is almost en-

tirely dielectric so we expect $\eta = 3$. The measured heat capacity is about a factor of 3 larger than predicted (see section III). Even without electro-thermal feedback, TKIDs are still fast enough for our targeted science band. There are indications that our dry release process using XeF_2 contributes to the excess heat capacity and that using a wet release process could lead to faster bolometers for space-based applications.

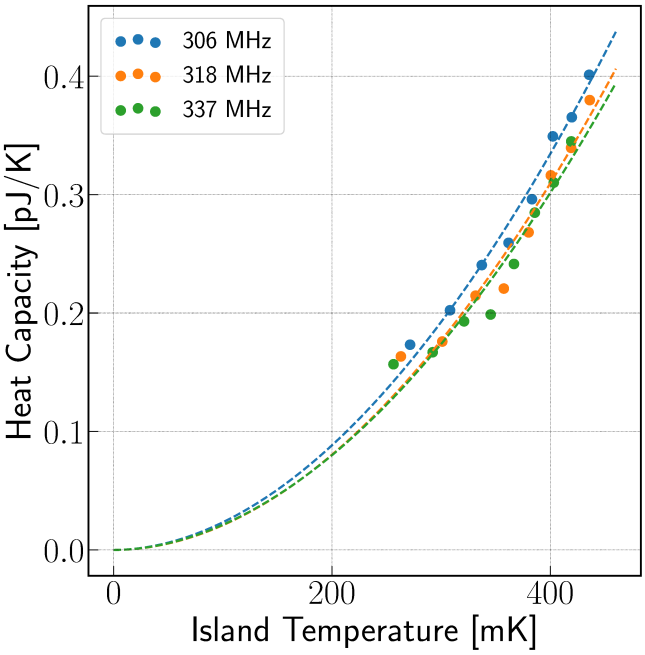

FIG. 9. Heat capacity for 3 TKID bolometers as a function of the island temperature. All three bolometers have similar heat capacities despite having different leg lengths showing that the island volume is the dominant contribution to the total heat capacity of the bolometer.

D. Responsivity

The bolometer responsivity as a function of the power dissipated on the island is the slope of the heater power vs. resonant frequency curve. Our theoretical estimates from the measured device parameters slightly underestimate the responsivity. Over large ranges of the optical power, the responsivity of a TKID bolometer is non constant. However, during normal CMB observations, the change in optical power is usually small with about a 2% variation in optical power. In this regime, the responsivity can be approximated as being constant with a small non-linearity correction on the order of a few percent. The level of non-linearity is similar to that of semi-conducting NTD Ge bolometers that operate with small correction factors[38,39].

E. Noise Performance

All the noise measurements were made by acquiring timestreams of the complex transmission of the resonators at fixed tone frequencies. The noise level was measured from 10 minutes of constant-bias data. A low noise, highly stable, Lakeshore 121 current source was used to DC bias the heater resistors. All the noise measurements were made at a 100 MHz native sample rate and flat-averaged in 1000 sample blocks to 100kHz. The power spectra of the resonance frequency timestream were estimated using the Welch method with a Hann window and 50% overlap. In order to convert from power spectra in frequency units to NEP, we directly measured the responsivity in short calibration noise acquisitions by modulating the DC bias with a 1% 1 Hz square wave for 10 seconds. The responsivity is then estimated as the ratio of the change in frequency to the change in power dissipated.

All our noise measurements were made with a bath temperature of 80 mK and not at 250 mK because at higher bath temperatures the UC stage temperature drifts significantly over the duration of the noise measurements. For the same achieved island temperature, we expect a 30% increase in the phonon noise for a 250 mK bath temperature due to the change in the temperature gradient across the bolometer leg. The measurement results presented here are focused on the 337 MHz resonator. To simulate the pair differencing that we usually do when making on-sky polarization measurements, we subtracted out all the noise that was common-mode with the other resonators being observed as shown in figure 10. The origin of the common-mode signal, which is not intrinsic to the detector, is still under investigation but may arise from e.g thermal fluctuations or RFI susceptibility. From the cleaned time-stream we computed the NEP at 4pW and 10pW heater bias levels.At both 4 pW and 10 pW loading levels, the total noise is lower than the photon noise level. This shows that the devices are background limited. The results and the predicted noise curves are given in figures 11-12. Given the lower bath temperature, the island temperature at 4 and 10 pW loading is 320 mK and 422 mK respectively. These 2 measurements demonstrate the two regimes in which gr noise or phonon noise is the dominant noise term.

Our noise predictions are largely limited by our knowledge of the quasiparticle recombination constant, R. The noise predictions were made with $R = 2.1\ \mu m^3 s^{-1}$, which matches the gr noise roll-off seen at 4 pW loading. However, as a result, the gr noise level is not well constrained. Future work will focus on further understanding the gr noise level and quasiparticle lifetimes in our devices.

VI. CONCLUSIONS

This paper presents a dark TKID design that has demonstrated background-limited performance for observing at 150 GHz and higher frequency bands for ground-based CMB polarimetry. We've described the fundamental theory of TKID bolometer performance and compared it to actual devices. Our devices are fabricated using Aluminum and Niobium films deposited on a Silicon wafer using standard lithography techniques. We also presented the results from measurements of the film properties, bolometer characterization and dark noise measurements. Our devices are well described us-

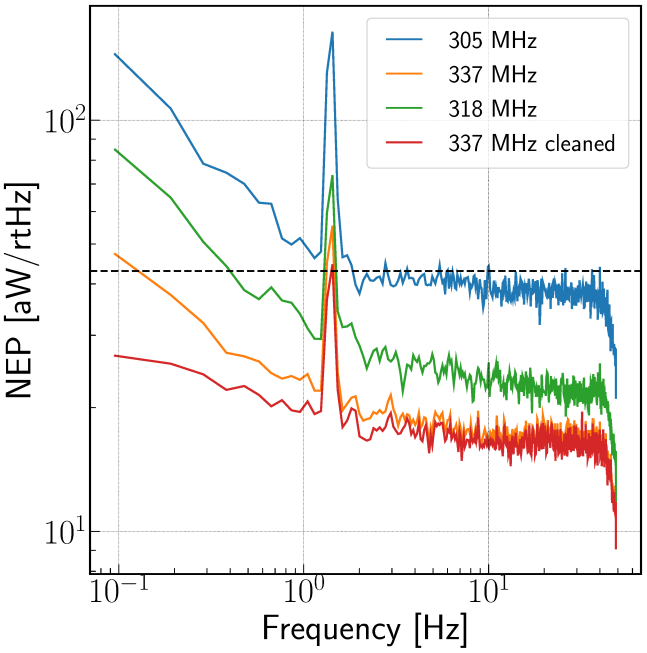

FIG. 10. NEP spectra for 3 TKID resonators with 4pW loading on the 337 MHz resonator. The red line shows the spectra with common mode subtraction suppressing the noise at low frequencies. The black dotted line shows the expected photon noise level at the South Pole in a band centered at 150 GHz with $\Delta\nu/\nu = 0.25$ and observing in 1 polarization from a ground-based site.

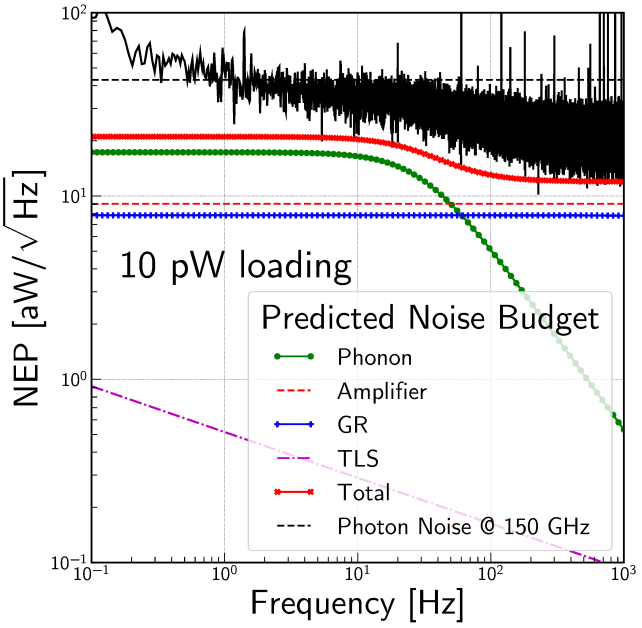

FIG. 12. NEPs of the 337 MHz resonator with a 10pW loading. The common mode noise has not been removed from the noise timestreams. Overplotted are the estimated phonon, generation-recombination and amplifier noise contributions to the total noise based on the measured device parameters. Phonon noise is the dominant term in the noise budget as evidenced by the clear phonon rolloff.

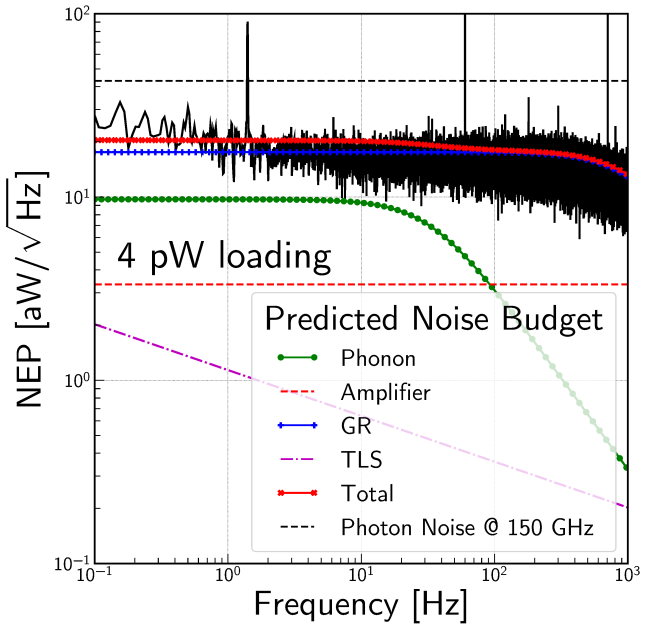

FIG. 11. NEPs of the 337 MHz resonator with a 4pW loading. The common mode noise has not been removed from the noise timestreams. Overplotted are the estimated phonon, generation-recombination and amplifier noise contributions to the total noise based on the measured device parameters. Below about 4.5 pW loading, we expect generation-recombination noise to dominate over the phonon noise

ing the Mattis-Bardeen theory at our operating temperature.

Future work will focus on further understanding quasiparticle lifetimes in our devices, increasing the number of devices and better understanding the common mode environmental noise in our measurement system. We will also work to better understand the performance of our devices under high cosmic ray backgrounds. As reported by several groups, arrays of KIDs can be susceptible to cosmic ray events[40,41]. Cosmic rays passing through a wafer generate ballistic phonons that propagate across the wafer, affecting multiple detectors. Cosmic rays thus cause extended dead-times because a single event affects multiple devices and because one must wait across several time constants for the response to decay. Cosmic ray susceptibility becomes even more important in space applications where event rates are significantly higher[42–44]. In TKIDs, the sensitive inductor is located on an island that is isolated from the entire wafer. The effective cross-section for interactions with cosmic rays is limited to the island instead of the entire wafer, greatly reducing our cosmic ray susceptibility. Other teams have reported similar results[40].

VII. ACKNOWLEDGEMENTS

The research was carried out at the Jet Propulsion Laboratory, California Institute of Technology, under contract with the National Aeronautics and Space Administration. We thank the JPL Research and Technology Development (RTD) pro-

gram for supporting funds, as well as the Dominic Orr Graduate Fellowship in Physics at Caltech for supporting Mr. Wandui's graduate research.

APPENDIX: DEFINITIONS OF VARIABLES

T	Temperature of the bolometer island.
$T_{\rm bath}$	Temperature of the thermal bath.
T_0	Target island operating temperature.
T_N	Noise temperature of the cold amplifier.
$C(T)$	Heat capacity of the bolometer at temperature T.
η	Power law index for the temperature dependence of the heat capacity.
$P_{\rm opt}$	Optical power absorbed on the island.
P_g	Microwave power of the readout tone used to excite the resonator.
$P_{\rm read}$	Readout power dissipated on the island.
$P_{\rm leg}$	Net heat flow from the island to the thermal bath.
$P_{\rm optimal}$	Optical power needed to raise the island temperature above $T_{\rm bath}$ to T_0.
$P_{\rm recomb}$	Average phonon power dissipated due to quasiparticle recombination.
K	Coefficient of thermal conductivity.
n	Power law index for the temperature dependence of the thermal conductivity.
$G(T)$	Thermal conductance of the thermal link between the island and the bath at an island temperature T.
$\delta P_{\rm opt}$	Perturbation to the optical power absorbed on the island.
δT	Perturbation to the island temperature due to a perturbation in the optical power $\delta P_{\rm opt}$.
$\delta n_{\rm qp}$	Perturbation to the quasiparticle density of the superconductor.
$\tau_{\rm bolo}$	Bolometer time constant.
χ	Bolometer flink factor in the phonon noise. Accounts for the temperature gradient across the leg.
$\nu_{\rm opt}$	Frequency at which the optical power is being detected.
$\Delta\nu_{\rm opt}$	Optical bandwidth.
ν	Frequency component of a fluctuating signal. The power spectrum is a function of this frequency.
f_r	Frequency of the resonance.
f	Frequency of the microwave tone used to readout the resonator.
$f_{\rm exc}$	Excitation frequency of probe signal used to bias the heater on the bolometer island.
$\dot{\theta}$	Rate at which the telescope scans across the sky while mapping the CMB.
$\theta_{\rm FWHM}$	Size of the beam of the telescope on the sky.
S_{21}	Forward scattering parameter of the resonator circuit.
Q_i	Internal quality factor of the resonator.
a	Bifurcation parameter for the resonator. For $a < 0.8$, the resonator is linear.
x	Fractional detuning of the probe frequency away from the resonance frequency. In the linear regime, $x = (f - f_r)/f_r$.
Q_e	Coupling quality factor of the resonator. Can be complex if the resonance is highly assymmetric. Measure of how the resonator is coupled to its external biasing circuit.
Q_r	Total quality factor of the resonator. Accounts for both losses internal to the resonator and losses due to the coupling of the resonator to its external bias circuit.
δ_r	$\delta_r = 1/Q_r$.
δ_e	$\delta_e = 1/Q_e$.
Q_c	Effective coupling quality factor of the resonator.
ϕ_c	Phase of Q_e.
χ_c	Coupling efficiency of the resonator. Equals 1 at optimum coupling when $Q_r = Q_c/2$.
χ_g	Detuning efficiency of the resonator. Equals 1 at zero detuning when $f = f_r$. $P_{\rm read} = 1/2 \cdot \chi_c \cdot \chi_g \cdot P_g$.
ϕ_g	Detuning phase of the resonator. $\tan\phi_g = 2Q_r x$, which vanishes at zero detuning.
δS_{21}	Perturbation in S_{21} of the resonator.
δx	Fractional change in to the resonance frequency corresponding to a measured perturbation in S_{21}.

δ_i	Change in to the dissipation of the resonator corresponding to a measured perturbation in S_{21}.
N_0	Single-spin density of states at the Fermi level.
T_c	Superconducting transition temperature.
Δ	BCS superconducting gap energy.
α_k	Kinetic inductance fraction of the resonator.
β	Ratio of the frequency response to a perturbation in the quasiparticle density to the dissipation response to the same perturbation.
n_{qp}	Total quasiparticle density of the superconductor accounting for all quasiparticle generation mechanisms.
n_{th}	Thermal quasiparticle density of the superconductor.
n^*_{qp}	Crossover density. Empirical measured constant that is the quasiparticle density below which the quasiparticle lifetime begins to saturate.
n_{bg}	Background quasiparticle density present in addition to the thermal quasiparticle density.
R	Recombination constant.
V_{sc}	Superconducting volume. $V = l \cdot w \cdot t$ for superconducting inductor length l, width w and thickness t.
τ_{qp}	Quasiparticle lifetime in the superconductor.
S	Responsivity of the TKID bolometer.
κ	Logarithmic responsivity of the quasiparticle density to changes in temperature.
κ_0	Empirical constant that sets the size of the TLS noise power.
F	Filling factor. Fraction of the total electrical energy of the resonator that is stored in the TLS hosting material.
δ_0	TLS loss tangent constant.
P_c	TLS critical power. Sets the power dependence of the shift in Q_i with changes in P_g.

VIII. REFERENCES

[1] H. Hui, P. A. R. Ade, Z. Ahmed, R. W. Aikin, K. D. Alexander, D. Barkats, S. J. Benton, C. A. Bischoff, J. J. Bock, R. Bowens-Rubin, J. A. Brevik, I. Buder, E. Bullock, V. Buza, J. Connors, J. Cornelison, B. P. Crill, M. Crumrine, M. Dierickx, L. Duband, C. Dvorkin, J. P. Filippini, S. Fliescher, J. Grayson, G. Hall, M. Halpern, S. Harrison, S. R. Hildebrandt, G. C. Hilton, K. D. Irwin, J. Kang, K. S. Karkare, E. Karpel, J. P. Kaufman, B. G. Keating, S. Kefeli, S. A. Kernasovskiy, J. M. Kovac, C.-L. Kuo, K. Lau, N. A. Larsen, E. M. Leitch, M. Lueker, K. G. Megerian, L. Moncelsi, T. Namikawa, C. B. Netterfield, H. T. Nguyen, R. O'Brient, R. W. Ogburn, S. Palladino, C. Pryke, B. Racine, S. Richter, R. Schwarz, A. Schillaci, C. D. Sheehy, A. Soliman, T. S. Germaine, Z. K. Staniszewski, B. Steinbach, R. V. Sudiwala, G. P. Teply, K. L. Thompson, J. E. Tolan, C. Tucker, A. D. Turner, C. Umiltà, A. G. Vieregg, A. Wandui, A. C. Weber, D. V. Wiebe, J. Willmert, C. L. Wong, W. L. K. Wu, E. Yang, K. W. Yoon, and C. Zhang, "Bicep array: a multi-frequency degree-scale cmb polarimeter," (2018).

[2] S. W. Henderson, R. Allison, J. Austermann, T. Baildon, N. Battaglia, J. A. Beall, D. Becker, F. De Bernardis, J. R. Bond, E. Calabrese, S. K. Choi, K. P. Coughlin, K. T. Crowley, R. Datta, M. J. Devlin, S. M. Duff, J. Dunkley, R. Dünner, A. van Engelen, P. A. Gallardo, E. Grace, M. Hasselfield, F. Hills, G. C. Hilton, A. D. Hincks, R. Hlozek, S. P. Ho, J. Hubmayr, K. Huffenberger, J. P. Hughes, K. D. Irwin, B. J. Koopman, A. B. Kosowsky, D. Li, J. McMahon, C. Munson, F. Nati, L. Newburgh, M. D. Niemack, P. Niraula, L. A. Page, C. G. Pappas, M. Salatino, A. Schillaci, B. L. Schmitt, N. Sehgal, B. D. Sherwin, J. L. Sievers, S. M. Simon, D. N. Spergel, S. T. Staggs, J. R. Stevens, R. Thornton, J. Van Lanen, E. M. Vavagiakis, J. T. Ward, and E. J. Wollack, "Advanced actpol cryogenic detector arrays and readout," Journal of Low Temperature Physics **184**, 772–779 (2016).

[3] Z. D. Kermish, P. Ade, A. Anthony, K. Arnold, D. Barron, D. Boettger, J. Borrill, S. Chapman, Y. Chinone, M. A. Dobbs, J. Errard, G. Fabbian, D. Flanigan, G. Fuller, A. Ghribi, W. Grainger, N. Halverson, M. Hasegawa, K. Hattori, M. Hazumi, W. L. Holzapfel, J. Howard, P. Hyland, A. Jaffe, B. Keating, T. Kisner, A. T. Lee, M. L. Jeune, E. Linder, M. Lungu, F. Matsuda, T. Matsumura, X. Meng, N. J. Miller, H. Morii, S. Moyerman, M. J. Myers, H. Nishino, H. Paar, E. Quealy, C. L. Reichardt, P. L. Richards, C. Ross, A. Shimizu, M. Shimon, C. Shimmin, M. Sholl, P. Siritanasak, H. Spieler, N. Stebor, B. Steinbach, R. Stompor, A. Suzuki, T. Tomaru, C. Tucker, and O. Zahn, "The polarbear experiment," (2012).

[4] B. A. Benson, P. A. R. Ade, Z. Ahmed, S. W. Allen, K. Arnold, J. E. Austermann, A. N. Bender, L. E. Bleem, J. E. Carlstrom, C. L. Chang, H. M. Cho, J. F. Cliche, T. M. Crawford, A. Cukierman, T. de Haan, M. A. Dobbs, D. Dutcher, W. Everett, A. Gilbert, N. W. Halverson, D. Hanson, N. L. Harrington, K. Hattori, J. W. Henning, G. C. Hilton, G. P. Holder, W. L. Holzapfel, K. D. Irwin, R. Keisler, L. Knox, D. Kubik, C. L. Kuo, A. T. Lee, E. M. Leitch, D. Li, M. McDonald, S. S. Meyer, J. Montgomery, M. Myers, T. Natoli, H. Nguyen, V. Novosad, S. Padin, Z. Pan, J. Pearson, C. Reichardt, J. E. Ruhl, B. R. Saliwanchik, G. Simard, G. Smecher, J. T. Sayre, E. Shirokoff, A. A. Stark, K. Story, A. Suzuki, K. L. Thompson, C. Tucker, K. Vanderlinde, J. D. Vieira, A. Vikhlinin, G. Wang, V. Yefremenko, and K. W. Yoon, "Spt-3g: a next-generation cosmic microwave background polarization experiment on the south pole telescope," (2014).

[5] M. Abitbol, A. M. Aboobaker, P. Ade, D. Araujo, F. Aubin, C. Baccigalupi, C. Bao, D. Chapman, J. Didier, M. Dobbs, S. M. Feeney, C. Geach, W. Grainger, S. Hanany, K. Helson, S. Hillbrand, G. Hilton, J. Hubmayr, K. Irwin, A. Jaffe, B. Johnson, T. Jones, J. Klein, A. Korotkov, A. Lee, L. Levinson, M. Limon, K. MacDermid, A. D. Miller, M. Milligan, K. Raach, B. Reichborn-Kjennerud, C. Reintsema, I. Sagiv, G. Smecher, G. S. Tucker, B. Westbrook, K. Young, and K. Zilic, "The EBEX balloon-borne experiment—detectors and readout," The Astrophysical Journal Supplement Series **239**, 8 (2018).

[6] K. N. Abazajian, P. Adshead, Z. Ahmed, S. W. Allen, D. Alonso, K. S. Arnold, C. Baccigalupi, J. G. Bartlett, N. Battaglia, B. A. Benson, C. A. Bischoff, J. Borrill, V. Buza, E. Calabrese, R. Caldwell, J. E. Carlstrom, C. L. Chang, T. M. Crawford, F.-Y. Cyr-Racine, F. De Bernardis, T. de Haan, S. di Serego Alighieri, J. Dunkley, C. Dvorkin, J. Errard, G. Fabbian, S. Feeney, S. Ferraro, J. P. Filippini, R. Flauger, G. M. Fuller,

V. Gluscevic, D. Green, D. Grin, E. Grohs, J. W. Henning, J. C. Hill, R. Hlozek, G. Holder, W. Holzapfel, W. Hu, K. M. Huffenberger, R. Keskitalo, L. Knox, A. Kosowsky, J. Kovac, E. D. Kovetz, C.-L. Kuo, A. Kusaka, M. Le Jeune, A. T. Lee, M. Lilley, M. Loverde, M. S. Madhavacheril, A. Mantz, D. J. E. Marsh, J. McMahon, P. D. Meerburg, J. Meyers, A. D. Miller, J. B. Munoz, H. N. Nguyen, M. D. Niemack, M. Peloso, J. Peloton, L. Pogosian, C. Pryke, M. Raveri, C. L. Reichardt, G. Rocha, A. Rotti, E. Schaan, M. M. Schmittfull, D. Scott, N. Sehgal, S. Shandera, B. D. Sherwin, T. L. Smith, L. Sorbo, G. D. Starkman, K. T. Story, A. van Engelen, J. D. Vieira, S. Watson, N. Whitehorn, and W. L. Kimmy Wu, "CMB-S4 Science Book, First Edition," arXiv e-prints , arXiv:1610.02743 (2016), arXiv:1610.02743 [astro-ph.CO].

[7] J. Zmuidzinas, "Superconducting microresonators: Physics and applications," Annual Review of Condensed Matter Physics **3**, 169–214 (2012), https://doi.org/10.1146/annurev-conmatphys-020911-125022.

[8] G. Ulbricht, B. A. Mazin, P. Szypryt, A. B. Walter, C. Bockstiegel, and B. Bumble, "Highly multiplexible thermal kinetic inductance detectors for x-ray imaging spectroscopy," Applied Physics Letters **106**, 251103 (2015), https://doi.org/10.1063/1.4923096.

[9] B. A. Steinbach, J. J. Bock, H. T. Nguyen, R. C. O'Brient, and A. D. Turner, "Thermal kinetic inductance detectors for ground-based millimeter-wave cosmology," Journal of Low Temperature Physics **193**, 88–95 (2018).

[10] J. C. Mather, "Bolometer noise: Nonequilibrium theory," Applied Optics **21** (1982).

[11] S. Pirro and P. Mauskopf, "Advances in bolometer technology for fundamental physics," Annual Review of Nuclear and Particle Science **67**, 161–181 (2017), https://doi.org/10.1146/annurev-nucl-101916-123130.

[12] J. C. Mather, "Bolometers: ultimate sensitivity, optimization, and amplifier coupling," Applied Optics **23** (1984).

[13] P. L. Richards, "Bolometers for infrared and millimeter waves," American Institute of Physics **76** (1994), 10.1063/1.357128.

[14] Although the inductor is superconducting, it has a non-zero AC resistance.

[15] P. A. R. Ade, R. W. Aikin, M. Amiri, D. Barkats, S. J. Benton, C. A. Bischoff, J. J. Bock, J. A. Bonetti, J. A. Brevik, I. Buder, E. Bullock, G. Chattopadhyay, G. Davis, P. K. Day, C. D. Dowell, L. Duband, J. P. Filippini, S. Fliescher, S. R. Golwala, M. Halpern, M. Hasselfield, S. R. Hildebrandt, G. C. Hilton, V. Hristov, H. Hui, K. D. Irwin, W. C. Jones, K. S. Karkare, J. P. Kaufman, B. G. Keating, S. Kefeli, S. A. Kernasovskiy, J. M. Kovac, C. L. Kuo, H. G. LeDuc, E. M. Leitch, N. Llombart, M. Lueker, P. Mason, K. Megerian, L. Moncelsi, C. B. Netterfield, H. T. Nguyen, R. O'Brient, R. W. O. IV, A. Orlando, C. Pryke, A. S. Rahlin, C. D. Reintsema, S. Richter, M. C. Runyan, R. Schwarz, C. D. Sheehy, Z. K. Staniszewski, R. V. Sudiwala, G. P. Teply, J. E. Tolan, A. Trangsrud, R. S. Tucker, A. D. Turner, A. G. Vieregg, A. Weber, D. V. Wiebe, P. Wilson, C. L. Wong, K. W. Yoon, and J. Zmuidzinas, "Antenna-Coupled TES Bolometers used in BICEP2, Keck Array, and SPIDER," The Astrophysical Journal **812**, 176 (2015).

[16] M. Tinkham, *Introduction to superconductivity / Michael Tinkham* (McGraw-Hill New York, 1996) pp. xix, 454 p. :.

[17] C. M. Wilson and D. E. Prober, "Quasiparticle number fluctuations in superconductors," Phys. Rev. B **69**, 094524 (2004).

[18] H. McCarrick, D. Flanigan, G. Jones, B. R. Johnson, P. Ade, D. Araujo, K. Bradford, R. Cantor, G. Che, P. Day, S. Doyle, H. Leduc, M. Limon, V. Luu, P. Mauskopf, A. Miller, T. Mroczkowski, C. Tucker, and J. Zmuidzinas, "Horn-coupled, commercially-fabricated aluminum lumped-element kinetic inductance detectors for millimeter wavelengths," Review of Scientific Instruments **85**, 123117 (2014), https://doi.org/10.1063/1.4903855.

[19] J. Gao, M. Daal, A. Vayonakis, S. Kumar, J. Zmuidzinas, B. Sadoulet, B. A. Mazin, P. K. Day, and H. G. Leduc, "Experimental evidence for a surface distribution of two-level systems in superconducting lithographed microwave resonators," Applied Physics Letters **92**, 152505 (2008), https://doi.org/10.1063/1.2906373.

[20] G. Frossati, J. leG Gilchrist, J. C. Lasjaunias, and W. Meyer, "Spectrum of low-energy dipolar states in hydrated vitreous silica," Journal of Physics C: Solid State Physics **10**, L515–L519 (1977).

[21] J. Burnett, L. Faoro, and T. Lindström, "Analysis of high quality superconducting resonators: consequences for TLS properties in amorphous oxides," Superconductor Science and Technology **29**, 044008 (2016).

[22] A. N. Ramanayaka, B. Sarabi, and K. D. Osborn, "Evidence for universal relationship between the measured 1/f permittivity noise and loss tangent created by tunneling atoms," arXiv e-prints , arXiv:1507.06043 (2015), arXiv:1507.06043 [cond-mat.supr-con].

[23] A. L. Burin, S. Matityahu, and M. Schechter, "Low-temperature $1/f$ noise in microwave dielectric constant of amorphous dielectrics in josephson qubits," Phys. Rev. B **92**, 174201 (2015).

[24] G. Wang, V. Yefremenko, V. Novosad, A. Datesman, J. Pearson, G. Shustakova, R. Divan, C. Chang, J. McMahon, L. Bleem, A. T. Crites, T. Downes, J. Mehl, S. S. Meyer, and J. E. Carlstrom, "Thermal properties of silicon nitride beams below 1 kelvin," AIP Conference Proceedings **1219**, 75–82 (2010), https://aip.scitation.org/doi/pdf/10.1063/1.3402336.

[25] W. A. E. Phillips, *Amorphous Solids, Low-Temperature Properties* (Springer-Verlag Berlin Heidelberg, 1981) pp. xi, 179 p. :.

[26] R. Corruccini and J. Gniewek, "Specific heats and enthalpies of technical solids at low temperatures. a compilation from the literature," (1960).

[27] Sonnet Software, Inc, "High frequency electromagnetics software, sonnet release 14 user g (2013), [Online; accessed 13-January-2020].

[28] High Precision Devices, Inc., "Cryostat model 103 rainier," [Online; accessed 13-January-2020].

[29] Cryomech, "Pt407 cryocoolers," [Online; accessed 13-January-2020].

[30] Cosmic Microwave Technology Inc., "Citlf2 cryogenic low noise amplifier," [Online; accessed 13-January-2020].

[31] L. Minutolo, B. Steinbach, A. Wandui, and R. O'Brient, "A flexible gpu-accelerated radio-frequency readout for superconducting detectors," IEEE Transactions on Applied Superconductivity **29**, 1–5 (2019).

[32] R. Barends, J. Wenner, M. Lenander, Y. Chen, R. C. Bialczak, J. Kelly, E. Lucero, P. O'Malley, M. Mariantoni, D. Sank, H. Wang, T. C. White, Y. Yin, J. Zhao, A. N. Cleland, J. M. Martinis, and J. J. A. Baselmans, "Minimizing quasiparticle generation from stray infrared light in superconducting quantum circuits," Applied Physics Letters **99**, 113507 (2011), https://doi.org/10.1063/1.3638063.

[33] L. J. Swenson, P. K. Day, B. H. Eom, H. G. Leduc, N. Llombart, C. M. McKenney, O. Noroozian, and J. Zmuidzinas, "Operation of a titanium nitride superconducting microresonator detector in the nonlinear regime," Journal of Applied Physics **113**, 104501 (2013), https://doi.org/10.1063/1.4794808.

[34] M. S. Khalil, M. J. A. Stoutimore, F. C. Wellstood, and K. D. Osborn, "An analysis method for asymmetric resonator transmission applied to superconducting devices," Journal of Applied Physics **111**, 054510 (2012), https://doi.org/10.1063/1.3692073.

[35] D. J. Goldie and S. Withington, "Non-equilibrium superconductivity in quantum-sensing superconducting resonators," Superconductor Science and Technology **26**, 015004 (2012).

[36] P. J. de Visser, D. J. Goldie, P. Diener, S. Withington, J. J. A. Baselmans, and T. M. Klapwijk, "Evidence of a nonequilibrium distribution of quasiparticles in the microwave response of a superconducting aluminum resonator," Phys. Rev. Lett. **112**, 047004 (2014).

[37] J. Gao, J. Zmuidzinas, A. Vayonakis, P. Day, B. Mazin, and H. Leduc, "Equivalence of the Effects on the Complex Conductivity of Superconductor due to Temperature Change and External Pair Breaking," Journal of Low Temperature Physics **151**, 557–563 (2008).

[38] Pajot, F., Ade, P. A. R., Beney, J.-L., Bréelle, E., Broszkiewicz, D., Camus, P., Carabétian, C., Catalano, A., Chardin, A., Charra, M., Charra, J., Cizeron, R., Couchot, F., Coulais, A., Crill, B. P., Dassas, K., Daubin, J., de Bernardis, P., de Marcillac, P., Delouis, J.-M., Désert, F.-X., Duret, P., Eng, P., Evesque, C., Fourmond, J.-J., François, S., Giard, M., Giraud-Héraud, Y., Guglielmi, L., Guyot, G., Haissinski, J., Henrot-Versillé, S., Hervier, V., Holmes, W., Jones, W. C., Lamarre, J.-M., Lami, P., Lange, A. E., Lefebvre, M., Leriche, B., Leroy, C., Macias-Perez, J., Maciaszek, T., Maffei, B., Mahendran, A., Mansoux, B., Marty, C., Masi, S., Mercier, C., Miville-Deschenes, M.-A., Montier, L., Nicolas, C., Noviello, F., Perdereau, O., Piacentini, F., Piat, M., Plaszczynski, S., Pointecouteau, E., Pons, R., Ponthieu, N., Puget, J.-L., Rambaud, D., Renault, C., Renault, J.-C., Rioux, C., Ristorcelli, I., Rosset, C., Savini, G., Sudiwala, R., Torre, J.-P., Tristram, M., Vallée, D., Veneziani, M., and Yvon, D., "Planck pre-launch status: Hfi ground calibration," A&A **520**, A10 (2010).

[39] Planck Collaboration, Adam, R., Ade, P. A. R., Aghanim, N., Arnaud, M., Ashdown, M., Aumont, J., Baccigalupi, C., Banday, A. J., Barreiro, R.

B., Bartolo, N., Battaner, E., Benabed, K., Benoît, A., Benoit-Lévy, A., Bernard, J.-P., Bersanelli, M., Bertincourt, B., Bielewicz, P., Bock, J. J., Bonavera, L., Bond, J. R., Borrill, J., Bouchet, F. R., Boulanger, F., Bucher, M., Burigana, C., Calabrese, E., Cardoso, J.-F., Catalano, A., Challinor, A., Chamballu, A., Chary, R.-R., Chiang, H. C., Christensen, P. R., Clements, D. L., Colombi, S., Colombo, L. P. L., Combet, C., Couchot, F., Coulais, A., Crill, B. P., Curto, A., Cuttaia, F., Danese, L., Davies, R. D., Davis, R. J., de Bernardis, P., de Rosa, A., de Zotti, G., Delabrouille, J., Delouis, J.-M., Désert, F.-X., Diego, J. M., Dole, H., Donzelli, S., Doré, O., Douspis, M., Ducout, A., Dupac, X., Efstathiou, G., Elsner, F., Enßlin, T. A., Eriksen, H. K., Falgarone, E., Fergusson, J., Finelli, F., Forni, O., Frailis, M., Fraisse, A. A., Franceschi, E., Frejsel, A., Galeotta, S., Galli, S., Ganga, K., Ghosh, T., Giard, M., Giraud-Héraud, Y., Gjerløw, E., González-Nuevo, J., Górski, K. M., Gratton, S., Gruppuso, A., Gudmundsson, J. E., Hansen, F. K., Hanson, D., Harrison, D. L., Henrot-Versillé, S., Herranz, D., Hildebrandt, S. R., Hivon, E., Hobson, M., Holmes, W. A., Hornstrup, A., Hovest, W., Huffenberger, K. M., Hurier, G., Jaffe, A. H., Jaffe, T. R., Jones, W. C., Juvela, M., Keihänen, E., Keskitalo, R., Kisner, T. S., Kneissl, R., Knoche, J., Kunz, M., Kurki-Suonio, H., Lagache, G., Lamarre, J.-M., Lasenby, A., Lattanzi, M., Lawrence, C. R., Le Jeune, M., Leahy, J. P., Lellouch, E., Leonardi, R., Lesgourgues, J., Levrier, F., Liguori, M., Lilje, P. B., Linden-Vørnle, M., López-Caniego, M., Lubin, P. M., Macías-Pérez, J. F., Maggio, G., Maino, D., Mandolesi, N., Mangilli, A., Maris, M., Martin, P. G., Martínez-González, E., Masi, S., Matarrese, S., McGehee, P., Melchiorri, A., Mendes, L., Mennella, A., Migliaccio, M., Mitra, S., Miville-Deschênes, M.-A., Moneti, A., Montier, L., Moreno, R., Morgante, G., Mortlock, D., Moss, A., Mottet, S., Munshi, D., Murphy, J. A., Naselsky, P., Nati, F., Natoli, P., Netterfield, C. B., Nørgaard-Nielsen, H. U., Noviello, F., Novikov, D., Novikov, I., Oxborrow, C. A., Paci, F., Pagano, L., Pajot, F., Paoletti, D., Pasian, F., Patanchon, G., Pearson, T. J., Perdereau, O., Perotto, L., Perrotta, F., Pettorino, V., Piacentini, F., Piat, M., Pierpaoli, E., Pietrobon, D., Plaszczynski, S., Pointecouteau, E., Polenta, G., Pratt, G. W., Prézeau, G., Prunet, S., Puget, J.-L., Rachen, J. P., Reinecke, M., Remazeilles, M., Renault, C., Renzi, A., Ristorcelli, I., Rocha, G., Rosset, C., Rossetti, M., Roudier, G., Rowan-Robinson, M., Rusholme, B., Sandri, M., Santos, D., Sauvé, A., Savelainen, M., Savini, G., Scott, D., Seiffert, M. D., Shellard, E. P. S., Spencer, L. D., Stolyarov, V., Stompor, R., Sudiwala, R., Sutton, D., Suur-Uski, A.-S., Sygnet, J.-F., Tauber, J. A., Terenzi, L., Toffolatti, L., Tomasi, M., Tristram, M., Tucci, M., Tuovinen, J., Valenziano, L., Valiviita, J., Van Tent, B., Vibert, L., Vielva, P., Villa, F., Wade, L. A., Wandelt, B. D., Watson, R., Wehus, I. K., Yvon, D., Zacchei, A., and Zonca, A., "Planck 2015 results - vii. high frequency instrument data processing: Time-ordered information and beams," A&A **594**, A7 (2016).

[40] K. Karatsu, A. Endo, J. Bueno, P. J. de Visser, R. Barends, D. J. Thoen, V. Murugesan, N. Tomita, and J. J. A. Baselmans, "Mitigation of cosmic ray effect on microwave kinetic inductance detector arrays," Applied Physics Letters **114**, 032601 (2019), https://doi.org/10.1063/1.5052419.

[41] A. D'Addabbo, M. Calvo, A. B. J. Goupy, O. Bourrion, A. C. aand J. F. Macias-Perez, and A. Monfardini, "High-energy interactions in kinetic inductance detectors arrays," (2014).

[42] Planck Collaboration, Ade, P. A. R., Aghanim, N., Armitage-Caplan, C., Arnaud, M., Ashdown, M., Atrio-Barandela, F., Aumont, J., Baccigalupi, C., Banday, A. J., Barreiro, R. B., Battaner, E., Benabed, K., Benoît, A., Benoit-Lévy, A., Bernard, J.-P., Bersanelli, M., Bielewicz, P., Bobin, J., Bock, J. J., Bond, J. R., Borrill, J., Bouchet, F. R., Bridges, M., Bucher, M., Burigana, C., Cardoso, J.-F., Catalano, A., Challinor, A., Chamballu, A., Chiang, H. C., Chiang, L.-Y, Christensen, P. R., Church, S., Clements, D. L., Colombi, S., Colombo, L. P. L., Couchot, F., Coulais, A., Crill, B. P., Curto, A., Cuttaia, F., Danese, L., Davies, R. D., de Bernardis, P., de Rosa, A., de Zotti, G., Delabrouille, J., Delouis, J.-M., Désert, F.-X., Diego, J. M., Dole, H., Donzelli, S., Doré, O., Douspis, M., Dupac, X., Efstathiou, G., Enßlin, T. A., Eriksen, H. K., Finelli, F., Forni, O., Frailis, M., Franceschi, E., Galeotta, S., Ganga, K., Giard, M., Girard, D., Giraud-Héraud, Y., González-Nuevo, J., Górski, K. M., Gratton, S., Gregorio, A., Gruppuso, A., Hansen, F. K., Hanson, D., Harrison, D., Henrot-Versillé, S., Hernández-Monteagudo, C., Herranz, D., Hildebrandt, S. R., Hivon, E., Hobson, M., Holmes, W. A., Hornstrup, A., Hovest, W., Huffenberger, K. M., Jaffe, A. H., Jaffe, T. R., Jones, W. C., Juvela, M., Keihänen, E., Keskitalo, R., Kisner, T. S., Kneissl, R., Knoche, J., Knox, L., Kunz, M., Kurki-Suonio, H., Lagache, G., Lamarre, J.-M., Lasenby, A., Laureijs, R. J., Lawrence, C. R., Leonardi, R., Leroy, C., Lesgourgues, J., Liguori, M., Lilje, P. B., Linden-Vørnle, M., López-Caniego, M., Lubin, P. M., Macías-Pérez, J. F., Mandolesi, N., Maris, M., Marshall, D. J., Martin, P. G., Martínez-González, E., Masi, S., Massardi, M., Matarrese, S., Matthai, F., Mazzotta, P., McGehee, P., Melchiorri, A., Mendes, L., Mennella, A., Migliaccio, M., Miniussi, A., Mitra, S., Miville-Deschênes, M.-A., Moneti, A., Montier, L., Morgante, G., Mortlock, D., Mottet, S., Munshi, D., Murphy, J. A., Naselsky, P., Nati, F., Natoli, P., Netterfield, C. B., Nørgaard-Nielsen, H. U., Noviello, F., Novikov, D., Novikov, I., Osborne, S., Oxborrow, C. A., Paci, F., Pagano, L., Pajot, F., Paoletti, D., Pasian, F., Patanchon, G., Perdereau, O., Perotto, L., Perrotta, F., Piacentini, F., Piat, M., Pierpaoli, E., Pietrobon, D., Plaszczynski, S., Pointecouteau, E., Polenta, G., Ponthieu, N., Popa, L., Poutanen, T., Pratt, G. W., Prézeau, G., Prunet, S., Puget, J.-L., Rachen, J. P., Racine, B., Reinecke, M., Remazeilles, M., Renault, C., Ricciardi, S., Riller, T., Ristorcelli, I., Rocha, G., Rosset, C., Roudier, G., Rusholme, B., Sanselme, L., Santos, D., Sauvé, A., Savini, G., Scott, D., Shellard, E. P. S., Spencer, L. D., Starck, J.-L., Stolyarov, V., Stompor, R., Sudiwala, R., Sureau, F., Sutton, D., Suur-Uski, A.-S., Sygnet, J.-F., Tauber, J. A., Tavagnacco, D., Terenzi, L., Toffolatti, L., Tomasi, M., Tristram, M., Tucci, M., Umana, G., Valenziano, L., Valiviita, J., Van Tent, B., Vielva, P., Villa, F., Vittorio, N., Wade, L. A., Wandelt, B. D., Yvon, D., Zacchei, A., and Zonca, A., "Planck 2013 results. x. hfi energetic particle effects: characterization, removal, and simulation," A&A **571**, A10 (2014).

[43] Catalano, A., Ade, P., Atik, Y., Benoit, A., Bréele, E., Bock „ J. J., Camus, P., Chabot, M., Charra, M., Crill, B. P., Coron, N., Coulais, A., Désert, F.-X., Fauvet, L., Giraud-Héraud, Y., Guillaudin, O., Holmes, W., Jones, W. C., Lamarre, J.-M., Macías-Pérez, J., Martinez, M., Miniussi, A., Monfardini, A., Pajot, F., Patanchon, G., Pelissier, A., Piat, M., Puget, J.-L., Renault, C., Rosset, C., Santos, D., Sauvé, A., Spencer, L. D., and Sudiwala, R., "Impact of particles on the planck hfi detectors: Ground-based measurements and physical interpretation," A&A **569**, A88 (2014).

[44] R. A. Mewaldt, A. J. Davis, K. A. Lave, R. A. Leske, E. C. Stone, M. E. Wiedenbeck, W. R. Binns, E. R. Christian, A. C. Cummings, G. A. de Nolfo, M. H. Israel, A. W. Labrador, and T. T. von Rosenvinge, "RECORD-SETTING COSMIC-RAY INTENSITIES IN 2009 AND 2010," The Astrophysical Journal **723**, L1–L6 (2010).

[45] C. L. Kuo, J. J. Bock, J. A. Bonetti, J. Brevik, G. Chattopadhyay, P. K. Day, S. Golwala, M. Kenyon, A. E. Lange, H. G. LeDuc, H. Nguyen, R. W. Ogburn, A. Orlando, A. Transgrud, A. Turner, G. Wang, and J. Zmuidzinas, "Antenna-Coupled TES Bolometer Arrays for CMB Polarimetry," (2008).

[46] W. A. Phillips, "Two-level states in glasses," Reports on Progress in Physics **50**, 1657–1708 (1987).

[47] H. Hui, P. A. R. Ade, Z. Ahmed, K. D. Alexander, M. Amiri, D. Barkats, S. J. Benton, C. A. Bischoff, J. J. Bock, H. Boenish, R. Bowens-Rubin, I. Buder, E. Bullock, V. Buza, J. Connors, J. P. Filippini, S. Fliescher, J. A. Grayson, M. Halpern, S. Harrison, G. C. Hilton, V. V. Hristov, K. D. Irwin, J. Kang, K. S. Karkare, E. Karpel, S. Kefeli, S. A. Kernasovskiy, J. M. Kovac, C. L. Kuo, E. M. Leitch, M. Lueker, K. G. Megerian, V. Monticue, T. Namikawa, C. B. Netterfield, H. T. Nguyen, R. O'Brient, R. W. O. IV, C. Pryke, C. D. Reintsema, S. Richter, R. Schwarz, C. Sorensen, C. D. Sheehy, Z. K. Staniszewski, B. Steinbach, G. P. Teply, K. L. Thompson, J. E. Tolan, C. Tucker, A. D. Turner, A. G. Vieregg, A. Wandui, A. C. Weber, D. V. Wiebe, J. Willmert, W. L. K. Wu, and K. W. Yoon, "Bicep3 focal plane design and detector performance," (2016).